Corrosion Science 143 (2018) 46–55

Contents lists available at ScienceDirect

Corrosion Science

journal homepage: www.elsevier.com/locate/corsci

Improvement of corrosion resistance of AA2024-T3 using femtosecond laser peening without protective and confining medium

Uroš Trdan[a,*], Tomokazu Sano[b], Damjan Klobčar[a], Yuji Sano[c], Janez Grum[a], Roman Šturm[a]

[a] *Faculty of Mechanical Engineering, University of Ljubljana, Aškerčeva 6, 1000 Ljubljana, Slovenia*
[b] *Division of Materials and Manufacturing Science, Graduate School of Engineering, Osaka University, 2-1 Yamada-oka, Suita, Osaka 565-0871, Japan*
[c] *Japan Science and Technology Agency, K's-gobancho, 7, Gobancho, Chiyoda-ku, Tokyo, 102-0076, Japan*

ARTICLE INFO

Keywords:
A. Aluminium
B. Polarization
B. SEM
C. Intergranular corrosion
C. Pitting corrosion

ABSTRACT

This work reports for the first time the effect of femtosecond laser shock peening (fLSP) without a sacrificial overlay under atmospheric conditions (no confinement) on the corrosion behaviour of AA2024-T3. After fLSP and additional exposure to air a superhydrophobic state ($\theta = 160 \pm 4^{\circ}$) is achieved. Moreover, fLSPed corrosion-resistant surface contributes to increased polarization resistance, reduced corrosion current and lower anodic dissolution, with long-term stability in aggressive chloride solution. Furthermore, SEM/EDS characterisation reveals reduction in pitting and complete eradication of intergranular corrosion (IGC) attack due to reduced metal/electrolyte contact area and homogeneous, refined microstructure which prevents chain-link IGC propagation.

1. Introduction

High-strength aluminium alloys are widely used in the transport and aerospace industries for various applications, e.g., fuselages, trailing edge panels, dorsal fins, etc., especially due to their good strength/weight and load capacity/weight ratios and their high mechanical properties [1,2]. However, AA2024-T3 remains one of the most studied aluminium alloys in the scientific corrosion literature due to its poor corrosion resistance in chloride-containing aqueous environments [3,4]. High corrosion susceptibility to localised corrosion, such as pitting and intergranular corrosion (IGC), originates from its complex heterogeneous microstructure with compositional variation, which leads to strong micro-galvanic coupling between various alloy phases [4–8].

Although Cu-rich particles, such as S–Al_2CuMg phase, θ–Al_2Cu phase, Guinier–Preston–Bagaryatsky (GPB) zones, S″ and S′ phase, produced by the matrix precipitation during solute segregation and ageing processes, highly improves the strength of the alloy, at the same time drastically increase pitting and IGC susceptibility [9]. Since S-phase with the corrosion potential of −920 mV (in a 0.5 M NaCl solution) [10] is more active than the surrounding matrix phase, severe dealloying by dissolution of Al and Mg may occur, resulting in the formation of Cu-rich particle remnants, which then behave as the noble sites [12]. Although, S-phases dealloy preferentially, also at the same time dealloying of the θ-phase, with corrosion potential of −700 mV [10], occurs by selective dissolution of Al from the θ-phase resulting in porous Cu-rich θ-phase remnants, comprised of randomly oriented metallic copper particles and copper oxides with sizes of 10–50 nm [11].

Moreover, due to the microstructural complexity and various intermetallic phases in the AA2024 alloy, corrosion is extremely stochastic, and there is still an open debate on the precise role of specific intermetallic phases, which also depend on the temper condition [4,13,14].

Since IGC attack can eventually lead to cracks and complete collapse of the structures, this must be avoided in industry and can be achieved with various protective coatings [15–17], corrosion inhibitors [18–20] or severe plastic deformation (SPD) methods to obtain a refined, more homogeneous microstructure with higher grain boundary volume fractions and redistributed Cu-rich precipitates [7,9,21]. However, one should note that microstructural alteration by SPD can be complex and challenging since it is reflected in changes in grain size, dislocation density, particle fragmentation, solute rearrangement and redistribution, which all drastically affect corrosion activity [7].

Laser shock peening or laser peening (LSP/LP) is a rapidly emerging and competitive SPD surface modification technique that generates laser-driven shock waves resulting in local plastic deformation, which in turn improves material properties with considerably deeper compressive residual stresses compared to traditional shot peening [22–24]. LSP using nanosecond (ns) laser pulses, which can be applied with or

---

[*] Corresponding author.
E-mail address: uros.trdan@fs.uni-lj.si (U. Trdan).

https://doi.org/10.1016/j.corsci.2018.08.030
Received 17 April 2018; Received in revised form 26 July 2018; Accepted 7 August 2018

without a protective/sacrificial coating at the laser–matter interaction zone, depending on the characteristics of the different laser sources, has already been recognised as an advanced and efficient surface treatment technique to improve several aspects of the treated material, e.g., mechanical properties [25,26], wear resistance [27,28], fatigue strength [29–32] and corrosion resistance [33–38].

Our previous studies [34,36] have already confirmed nanosecond LSP (ns-LSP) without coating as an effective surface treatment to improve corrosion resistance of precipitation-hardened AA6082-T651 alloy. Results have confirmed enhanced passivity, 7-times higher polarization resistance R_p with lower double-layer capacitance C_{dl}, due to the high density of dislocations and compressive residual stress [39] and a modified/thicker, more stable, passive oxide film [36]. Krawiec et al. [40] also demonstrated a sharp increase in the charge transfer and oxide film resistances at sites containing the matrix with AA2050-T8 alloy, due to the development of compressive stresses during ns-LSP. Lu et al. [37] showed that massive ns-LSP treatment can greatly improve resistance to stress corrosion cracking and electrochemical properties in a 0.598 M NaCl solution, whereas higher pulse energy contributes to higher corrosion resistance. Moreover, Karthik et al. [41] reported significantly improved corrosion resistance after massive ns laser peening without coating with 19-times lower corrosion rate and 5-times higher charge-transfer resistance R_{ct} compared to the untreated material.

Nonetheless, with all ns-LSP processes it is essential to cover the surface with a confining transparent medium (water, glass) to suppress plasma expansion which in turn produces sufficient shock-wave generation to deform the material plastically [23,30]. In contrast, femtosecond LSP (fLSP) is opening new possibilities of direct laser irradiation under atmospheric conditions without sacrificial overlay, which makes it a more economic and cleaner technology, producing lower waste gas emissions. Although the energy of the fs pulse is low, the extremely short pulse width reflects in extremely high intensity, sufficient to produce intense shock waves even in air [42], producing metastable high-pressure phases [43,44], dense dislocation configurations [45,46] and compressive residual stresses [24]. Moreover, despite intensive research efforts [47,48] devoted to fs laser texturing to obtain multifunctional hierarchical superhydrophobic surfaces, the effect of fs LSP using high laser fluence in excess of 10 Jcm^{-2} to drive a strong shock wave propagating into the material, corrosion and superhydrophobic developments have never been reported.

Hence, the purpose of this work is to study how fLSP without protective and confining medium performed in air affects mechanical properties via nanoindentation and residual stress measurements, wettability and electrochemical properties of aeronautical AA2024-T3 alloy in a chloride environment. Corrosion was evaluated using potentiodynamic linear and cyclic polarization CP) and electrochemical impedance spectroscopy (EIS), whereas the specific attention was focused on determining the long-term stability and durability of pre-corroded samples after longer immersion times. In addition, the effect of surface ablation and fs laser-driven shock waves on the intensity of pitting and IGC attack was examined using SEM/EDS analyses.

2. Material and methods

2.1. Material and femtosecond laser shock peening

In this study 15 mm discs were cut using an electric discharge machine from 3 mm thick plates of commercial aluminium alloy AA2024-T3. Table 1 shows the chemical composition in wt.% of this aluminium alloy. The surface of the specimen to be irradiated by fLSP treatment was electropolished in 20% sulphuric acid/methanol electrolyte for 30 s to remove the work-strained layer.

Fig. 1 illustrates schematically the experimental setup for femtosecond laser peening. The specimen of AA2024-T3 was mounted on an x–y stage as shown in Fig. 1a. Femtosecond laser pulses (Spectra-Physics Inc., Spitfire) with a wavelength of 800 nm, a pulse width of 120 fs and pulse energy of 0.6 mJ were focused using a plano-convex lens with a focal length of 70 mm and irradiated normal to the electropolished surface of the specimen in air.

Table 1
Chemical composition in wt.% of AA2024-T3 used in this study.

Cu	Mg	Mn	Fe	Si	Zn	Ti	Others	Al
4.4	1.4	0.55	0.05	0.02	0.02	0.01	0.01	Bal.

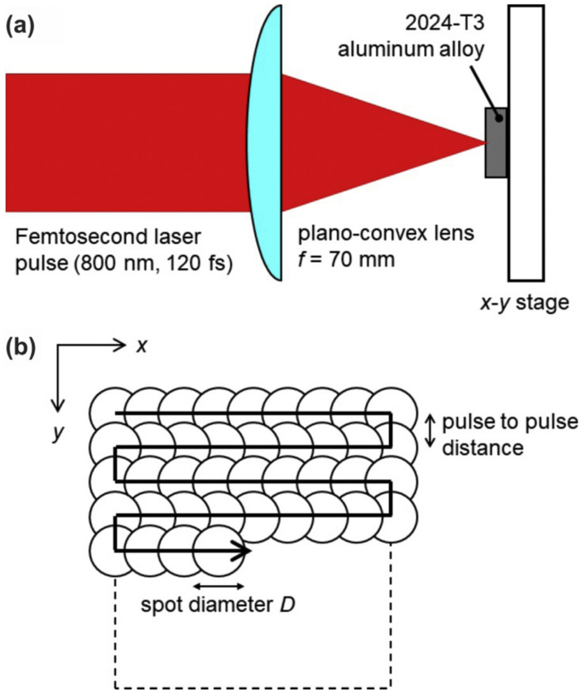

Fig. 1. Schematic illustrations of (a) experimental setup for laser irradiation and (b) scan direction of laser pulses for the setup shown in (a).

For the peening treatment, the aluminium specimen was moved in the x- and y-directions during laser irradiation as shown in Fig. 1b to be irradiated with a coverage C_v of 692% which is expressed by $C_v = \pi D^2 N_p/4$ where D is the spot diameter of the laser pulse irradiated and N_p is the number of pulses per unit square.

2.2. Surface morphology, nanoindentation and residual stress measurements

Surface morphology of the femtosecond laser-peened aluminium alloy was observed using a Hitachi S-3000H scanning electron microscope (SEM). Measurement of surface roughness was performed using a Keyence VK-9700 laser microscope with a wavelength of 408 nm and a depth resolution of 0.05 um.

The residual stress on the femtosecond laser-peened surface was estimated from the Al(311) diffraction peak of CrKα X-rays (2.2897 Å) using a Young's modulus of 70.3 GPa and a Poisson's ratio of 0.345. Thin layers of the surface were successively removed by repeated stepwise electrolytic polishing using 10% $HClO_4$ solution at an applied voltage of 16 V to obtain the depth profile of the residual stress. The removed thickness was determined from the step difference between unremoved and removed areas measured using a laser microscope. The hardness of the cross-section was measured by an Elionix ENT-1100a nanoindentation system with the applied load of 1 mN. Before the nanoindentation measurements, the cross-section was polished by a JEOL SM-09010 using a 5 keV Ar-ion beam to remove the work-hardened layer.

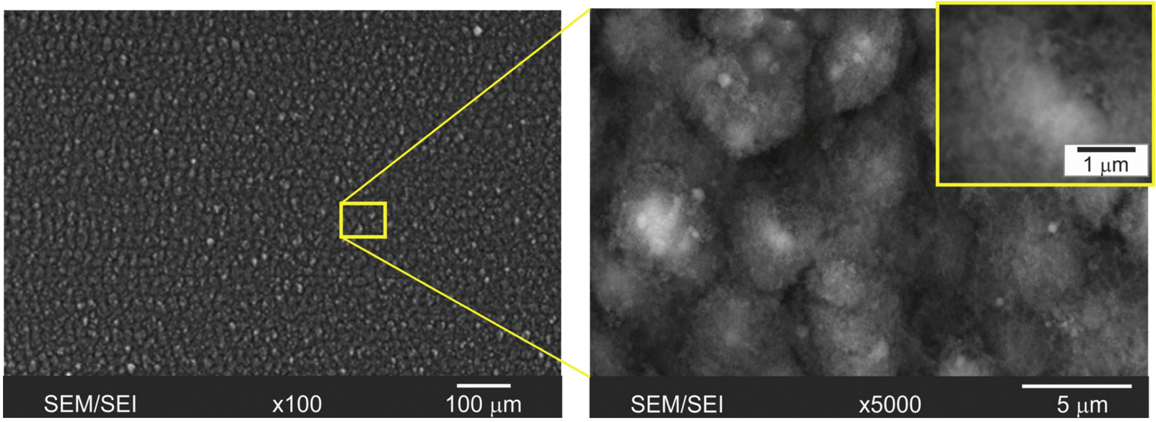

Fig. 2. SEM images of the surface of AA2024-T3 sample after femtosecond laser peening.

2.3. Wettability and electrochemical measurements

The hydrophobicity, i.e. water repellency, of the samples was studied by a static contact angle (SCA) measurement, using the a goniometer of our own design, where a droplet of distilled water with a volume of 5 µL was delivered to the investigated surface [49,50]. The measurements on base material (BM) and fLSPed samples were conducted after exposure to ambient conditions (T = 23 °C, RH = 35%) for one month, where prior to SCA measurements both samples were ultrasonically cleaned in distilled water and rinsed with ethanol.

Electrochemical measurements were carried out with a PAR Versastat-4 potentiostat/galvanostat/ZRA using a three-electrode corrosion cell under static conditions, with a saturated calomel electrode (SCE) as a reference and a graphite rod as a counter electrode. Immediately prior to each corrosion experiment, all specimens were cleaned and degreased in an ultrasonic bath of ethanol followed by deionised water for 3 min each, dried under a stream of warm air and embedded in a Teflon PAR holder as the working electrode (1 cm^2). The test medium was a naturally aerated (T = 22 ± 1 °C) 0.6 M NaCl solution, freshly prepared with deionised water before each experiment.

Afterwards, the samples were immersed in the solution and open circuit potential measurements ($E_{ocp} = f[t]$) were performed for 60 min in order to stabilise the surface, and corrosion potential E_{corr}, was determined at the end of the stabilisation process. Followed by OCP, linear polarization resistance (LPR) measurements were performed in the potential range ± 10 mV relative to E_{corr} using 0.1 mVs^{-1} potential scan rate. The EIS measurements were performed after the LPR measurements and prior to the cyclic polarization (CP) scans [51,52] at steady free corrosion potential (E_{corr}) by applying a sinusoidal 10 mV RMS perturbation signal at frequencies ranging from 50 kHz down to 100 mHz. Impedance data was experimentally determined by fitting, using an equivalent electrical circuit with ZsimpWin software.

CP scans were performed after the EIS measurements. CP was conducted in the anodic direction with a scan rate of 1 mV/s, starting at −150 mV vs. E_{corr}. The polarization direction was reversed at the switching potential E_{sw} at which the potential reached a limited threshold value of 1 mAcm^{-2} and progressed in the cathodic direction towards the starting potential. The consistency of consecutive electrochemical measurements was ensured by repeating all experiments twice with different samples prepared by the same parameters in a freshly prepared electrolyte solution, and as a result a representative curve was selected.

To evaluate surface condition and corrosion morphology after the CP tests, each specimen was cleaned ultrasonically in alcohol, rinsed gently with deionised water, dried and stored in a desiccator. Samples for cross-section examination of the microstructure and intensity of IGC attack after CP were cut along the LT–ST plane using a diamond saw followed by hot mounting and polishing to a mirror finish (0.04 µm colloidal silica suspension) and etching with Keller's reagent. The surface condition, microstructure and chemical composition of the surface after CP were examined using a JEOL JSM-5610 SEM microscope equipped with EDS microanalysis hardware. Acceleration voltage during SEM experiments was kept constant at 20 kV.

In order to investigate long-term stability against corrosion and to obtain insights into the active-passive behaviour, the formation of corrosion products and the durability in aggressive chloride solution, additional electrochemical measurements were carried out on pre-corroded surfaces after CP and exposure to air under ambient conditions for six months. Here, EIS measurements (using the same configuration as described above) were performed after 24 h immersion at OCP. All electrochemical corrosion techniques were pre-tested to ensure the repeatability of the experiments.

3. Results and discussion

3.1. The effect of fLSP on surface morphology and mechanical properties

Fig. 2 shows the SEM images of the femtosecond laser-peened surface of the AA2024-T3 with multidirectional structures as a consequence of constant melting, ablation and deposition of the recast material during laser treatment. Nonetheless, droplets were not observed, indicating that the femtosecond laser treatment creates a negligibly small molten layer. The surface roughness R_a is 1.2 µm, which is more than 2-times lower than that of a nanosecond laser-peened [53] as well as shot-peened surface [54], respectively.

Fig. 3 depicts the residual stress along the x-direction σ_x and y-direction σ_y, and hardness as a function of depth from the surface. The

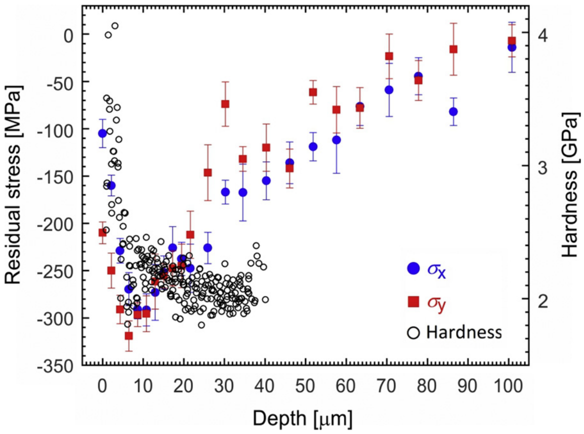

Fig. 3. Residual stress and hardness through-depth distribution of the femtosecond laser-peened AA2024-T3 sample.

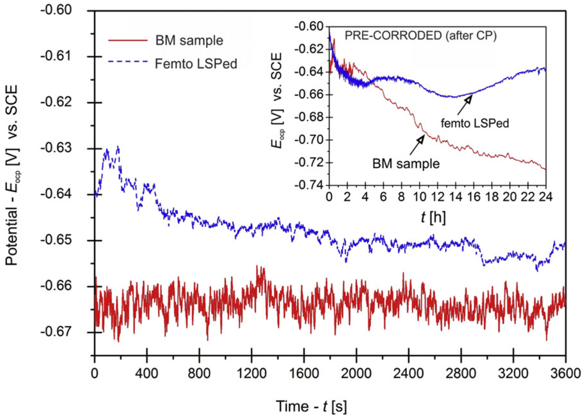

Fig. 4. Rest potential ($E_{ocp} = f[t]$) curves of BM and fLSP-treated AA2024-T3 sample (Inset: rest potential recordings at longer 24 h exposure time on pre-corroded samples after CP).

surface region within around 100 µm has a compressive residual stress for both x- and y-directions, of which maximum value is about 300 MPa at a depth of 6 µm, which is almost same as the 0.2% proof stress of AA2024-T3. The region within 6 µm from the surface with the most compressive residual stress corresponds to the most hardened region. The largest value of the hardness is almost twice that of the unpeened aluminium alloy with a hardness of 2.0 GPa, which indicates that local work-hardening or plastic deformation induces the compressive residual stress.

3.2. Electrochemical studies

3.2.1. Open circuit potential

The OCP curves ($E_{ocp} = f$[t]) of the femto laser-peened (fLSPed) and BM samples in a 0.6 M NaCl aqueous solution are depicted in Fig. 4. Potential-time transients indicate more anodic (positive) values of the fLSPed sample compared to the BM sample, with relatively stable potential values with lower fluctuations after approximately 30 min immersion in the test solution. The initial OCP values were –640 mV_{SCE} and –665 mV_{SCE} for fLSP and BM samples, respectively. Afterwards, a small gradual potential decrease with longer immersion time was observed, which after 1 h immersion achieved a potential of –650 mV_{SCE} and − 663 mV_{SCE}.

Similar results of small potential differences between LSPed and BM samples during 1 h immersion was also confirmed in our previous research [34,36] in which nanosecond laser peening without coating had been applied. Nonetheless, despite small E_{corr} ennoblement, the results confirmed improved corrosion resistance with smaller anodic dissolution and 12-times lower corrosion current compared to the untreated BM sample (0.14 ± 0.04 μAcm^{-2} vs. 1.76 ± 0.34 μAcm^{-2}) [36].

On the other hand, rest potential recording at a longer, 24 h, immersion time on pre-corroded samples after CP and exposure to air at ambient conditions for six months (inset in Fig. 4) showed a completely different situation. The fLSPed sample showed a more durable surface state, i.e. lower corrosion activity with 86 mV higher potential after 24 h immersion (− 638 mV_{SCE} vs. − 724 mV_{SCE}). Although both samples showed a similar descending trend in the initial 4 h immersion, afterwards with the fLSPed sample the potential shifted in the anodic direction and held a stable value over a longer duration. Furthermore, two distinctive regions of potential ennoblement could be observed with fLSPed sample, i.e. the first from 4 to 10 h and the second from 12 to 24 h immersion, whereas with BM sample a constant potential drop was observed. Such results imply higher resistance of fLSPed surface, with increased long-term stability during longer immersion in the corrosive environment. If this holds true it will be either confirmed or rejected by the wettability measurements, LPR, CP and EIS tests in the following sections.

Table 2
Characteristic parameters obtained from electrochemical measurements of BM and fLSPed AA2024-T3 sample in a 0.6 M NaCl: R_p from LPR, and E_{corr}, E_{sw}, E_{rp} and i_{corr} from CP curves.

Parameter	Sample/Condition	
	BM	fLSPed
R_p [kΩcm^2]	1.92 ± 0.23	34.83 ± 4.51
E_{corr} [mV_{SCE}]	−627 ± 7	−656 ± 12
E_{sw} [mV_{SCE}]	−568 ± 5	−508 ± 6
E_{rp} [mV_{SCE}]	−787 ± 11	−778 ± 8
β_a [mV/dec]	20 ± 5	29 ± 3
β_c [mV/dec]	−409 ± 32	−146 ± 18
i_{corr} [μA/cm^2]	1.95 ± 0.28	0.49 ± 0.07
R_{corr} [µm/year]	20.2 ± 2.9	5.1 ± 0.8
SCA [°]	89 ± 5°	160 ± 4°

3.2.2. Linear polarization resistance

LPR measurements were conducted after 1 h immersion at open circuit in the potential range ± 10 mV relative to E_{corr} using 0.1 mV/s scan rate. The values of polarization resistance R_p, determined from the slope of E–i curves [$R_p = (dE/di)$] are given in Table 2.

LPR analysis showed much smaller electric current variation in the given potential range with the fLSP-treated sample, with 18-times higher polarization resistance R_p value for the fLSP sample than the BM sample, i.e. 34.83 ± 4.51 kΩcm^2 vs. 1.92 ± 0.23 kΩcm^2. Furthermore, calculated values of protective efficiency ($P_{EF} = (R_p^{fLSP} - R_p^{BM})/R_p^{fLSP} \times 100$) indicate almost 95% higher resistance to corrosion in a 0.6 M NaCl solution after fLSP treatment as a consequence of surface ablation and generated shock waves [34,40].

3.2.3. Cyclic polarization and wettability measurements

In this section, electrochemical characteristics are analysed via CP curves to study active/passive behaviour and the propensity of material towards pitting corrosion [49,55]. CP curves of non-processed (BM) and fLSP AA2024-T3 samples with the insert of water droplets obtained during the wettability measurements (prior to corrosion experiments) are shown in Fig. 5.

The SCA measurements of the plain non-processed and non-polished Al surface indicate a hydrophilic state with SCA = 89 ± 5°, despite being exposed to ambient conditions for at least one month (or an even longer time, i.e. from the very production onward). On the other hand, the fLSPed sample exposed to ambient conditions for one month after laser treatment developed superhydrophobic properties in a Cassie-

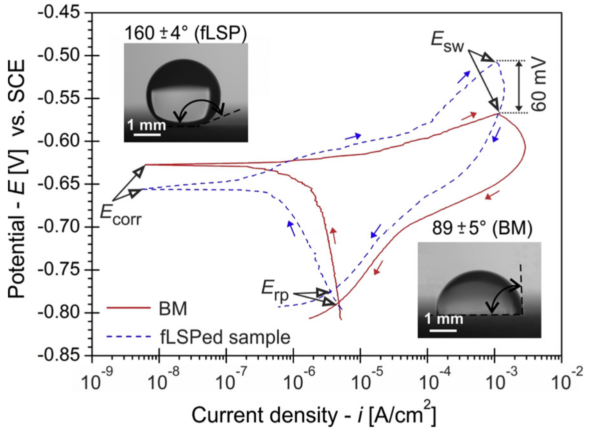

Fig. 5. Cyclic polarization (CP) curves in 0.6 M NaCl solution of BM and fLSPed AA2024-T3 samples (Inset: water droplet/contact angle measurement of BM and fLSPed samples prior to corrosion testing).

Baxter regime [56] with SCA = 160 ± 4°. However, it should be noted that immediately after laser treatment the entire surface was in a superhydrophilic [48,49,57], saturated state [58] of a Wenzel regime [59] with a contact angle SCA = 0°, so was more susceptible to corrosion than the base, unprocessed sample [50]. Nonetheless, after a given time (depending on several mechanisms, which are is still under debate [60] and not fully accepted to explain this behaviour [50]), superhydrophobicity within a nanostructured surface develops [48,50,61,62]. Therefore, in the scope of this research we will study how this transition to the superhydrophobic state of the fLSPed sample, which was achieved prior to immersion in electrolyte solution, influences the corrosion behaviour.

The various characteristic potentials, such as E_{corr}, E_{pit} and E_{rp} obtained from CP scans, are denoted in Fig. 5 and presented in Table 2, and their detailed description and definition are given in Ref. [50]. From the CP experimental results, a good correlation with the OCP and LPR measurements can be seen, indicating that after fLSP treatment superior corrosion resistance is achieved. Nonetheless, by comparing E_{ocp} and E_{corr} an opposite tendency can be seen. This is most likely associated with the sequence itself (OCP → LPR → EIS → CP). However, with the fLSPed sample a smaller difference between E_{ocp} and E_{corr} compared to the BM sample was obtained (15 mV vs. 38 mV) indicating more stable condition, with lower corrosion activity during LPR and EIS measurements.

Moreover, despite lower E_{corr} of the fLSPed sample (–656 ± 12 mV_{SCE} vs. –627 ± 7 mV_{SCE}) and a typical active behaviour in the forward (anodic) scan, the BM sample showed a wider hysteresis loop and, consequently more negative E_{rp} and lower E_{sw}, indicating higher susceptibility to localised corrosion attack. Moreover, corrosion current density i_{corr}, obtained via the Tafel extrapolating method confirm an almost 4-times lower value after fLSP treatment (1.95 ± 0.28 μAcm^{-2} vs. 0.49 ± 0.07 μAcm^{-2}). A similar trend was observed for corrosion rate (20.2 ± 2.9 $\mu myear^{-1}$ vs. 5.1 ± 0.8 $\mu myear^{-1}$) which was calculated according to Faraday's law [63] in accordance with ASTM G-59-97 standard [64] and by taking into account all the elements, their concentrations and valences that are being oxidised and contributing to corrosion [65].

To evaluate further the effect of fLSP treatment on the improvement against localised corrosion in a chloride-containing solution, ΔE trends [34,55] were determined and compared (Fig. 6). Results clearly demonstrate the beneficial effect of fLSP treatment towards improved corrosion resistance. Analysis confirm a lower degree of material anodic dissolution with 2.5-times larger E_{sw}– E_{corr} value (148 ± 9 mV vs. 59 ± 6 mV) and improved, faster repassivation with smaller E_{corr}– E_{rp} value (122 ± 10 mV vs. 160 ± 9 mV).

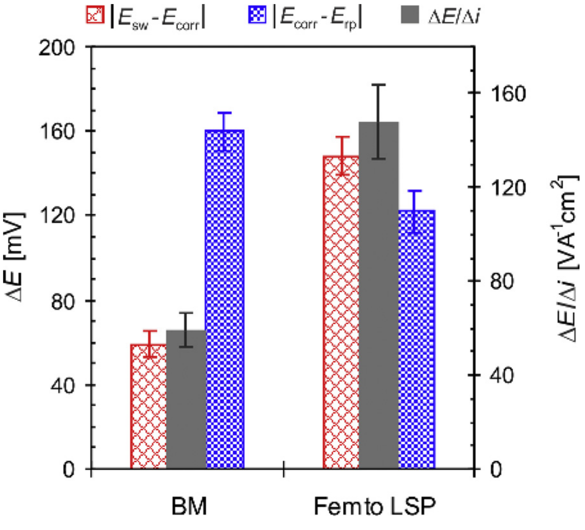

Fig. 6. Comparison of characteristic potentials $|E_{sw} - E_{corr}|$ and $|E_{corr} - E_{rp}|$ and anodic dissolution gradient ($\Delta E/\Delta i$) obtained from the CP tests in 0.6 M NaCl water solution.

Moreover, to obtain information about general resistance against anodic dissolution in a Cl^- solution, the $\Delta E/\Delta i$ gradient was also considered; ΔE represents the difference between two potentials $|E_{sw} - E_{corr}|$ and Δi corresponds to difference between the current density of the potentials [34]. A distinctive shift in $\Delta E/\Delta i$ gradient can be observed with the fLSP sample, with a more than 150% higher value compared to the BM sample.

Although during CP neither BM nor fLSPed samples showed the classical passive behaviour and that E_{corr} and E_{pit} were superimposed/coincided ($E_{corr} = E_{pit}$), all the above results clearly demonstrate the beneficial effect of fLSP treatment against corrosion. Increased corrosion resistance of the fLSPed specimen surface could be attributed to several possible effects produced during the fLSP process, e.g., extreme water repellency, a more stable and corrosion-resistant surface of lower capacitance, refined microstructure and generated compressive residual stresses in the surface layer.

Fig. 7 shows the surface condition of BM and fLSPed samples after polarization tests. Although, both samples confirm pitting attack, the untreated one shows inferior surface integrity with extensive, widespread localised corrosion attack in the form of surface-hemispherical and crystallographic pitting. In contrast, for the fLSPed sample, which was in a superhydrophobic state prior to corrosion testing, the pitting attack was almost eradicated and was mainly confined to few isolated regions (possible areas of non-homogeneity, i.e. fLSP-affected craters, etc.).

From the CP scans (Fig. 5) and SEM observations (Figs. 7–9) it seems that the developed superhydrophobicity with entrapped air reduces the fractional area of liquid–solid interface, as suggested by the Cassie-Baxter model [56], hence making the penetration of water molecules and halide ions to the surface more difficult [50,61]. EDS analysis of the top-surface regions (marked on Figs. 8a and 9 a) confirmed much smaller incorporation of Cl in the corrosion product on the fLSPed surface, with almost 2-times lower average chloride content than with BM sample (0.56 wt.% vs. 1.11 wt.%). In addition, insets in Fig.7a and c confirm thicker corrosion product with intensive cracks on the BM sample, which occurred due to dehydration after exposure to ambient conditions. In contrast, with the fLSPed sample fewer cracks were detected, indicating improved conditions, since cracks presents free paths into the interior of the material, which could promote local acidification and intense material dissolution if the sample were again exposed to a corrosive environment.

Figs. 8 and 9 show SEM/BEI micrographs of BM and fLSPed sample surfaces after CP, along with the EDS analysis results, respectively. On the top surface of the BM sample extensive pitting and IGC attack (Fig. 8b) can be seen, whereas with fLSP the surface condition is greatly improved with reduced pitting and no sign of IGC attack. The IGC attack after CP (Figs. 8d and 9 d) was additionally examined by metallographic cross-section observations in the LT-ST plane where the IGC was the most severe [7,9]. With the BM sample (Fig. 8d) several coarser, irregularly shaped Al-Cu-Fe-Mn and smaller S-phase (Al_2CuMg) particles can be seen with IGC penetration to a depth of approximately 30 μm from the surface. Although it is generally accepted that IGC in 2xxx alloys commence with the dissolution of S-phase (dealloying by dissolution of Al and Mg) on grain boundaries due to its active character and micro-galvanic coupling [7,9,12], beyond the pitting potential other effects prevail. Microstructural heterogeneity, active phases along grains, Cu-rich remnants, compositional variations between solute-depleted zone/matrix and solute-depleted zone/S-phase particles with strong galvanic coupling promote increase kinetics leading to 'chain-link' shaped IGC attack along the grain boundaries [5,7,11,14].

In contrast, the cross-sectional observations of the fLSPed sample (Fig. 9c and d) did not reveal any signs of IGC attack. Such improvement is associated with fLSP treatment, producing more homogeneous, refined microstructure on the top surface, with smaller amount and/or

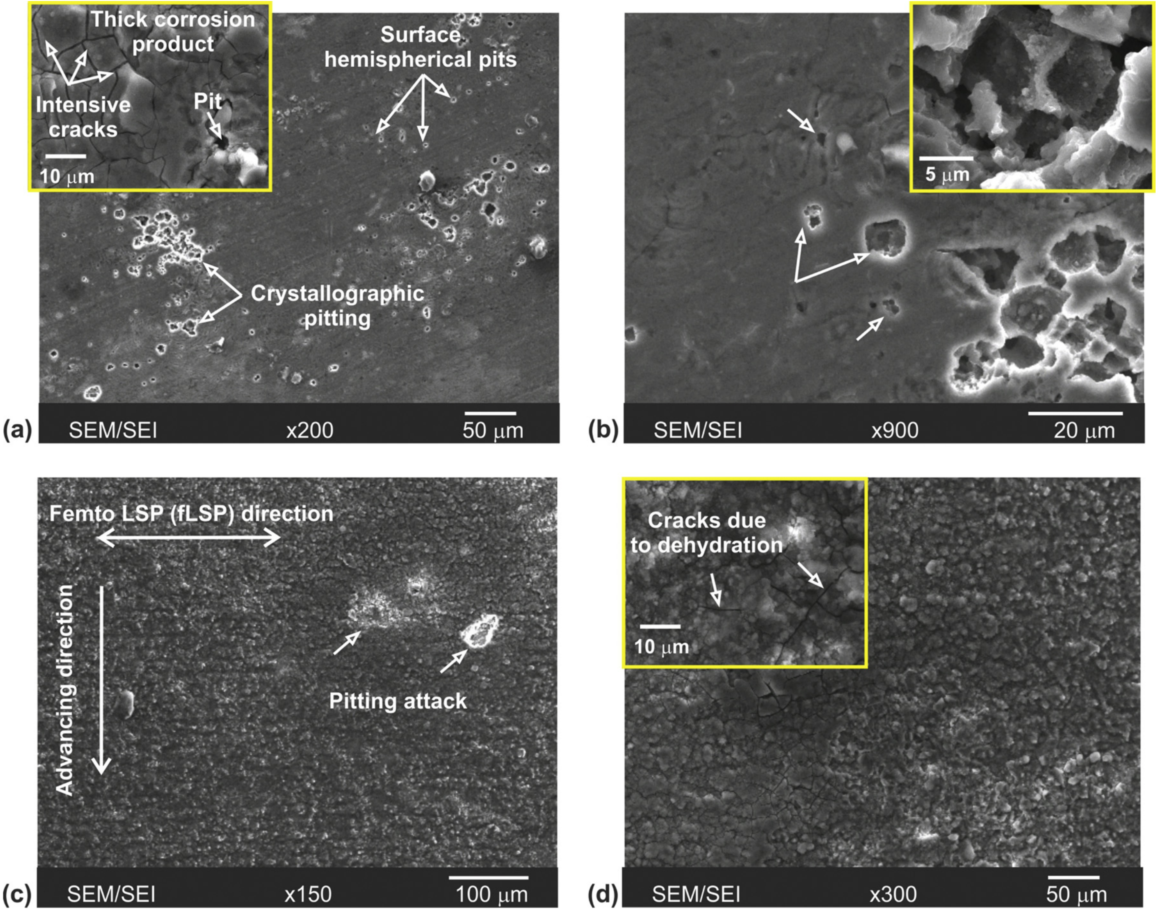

Fig. 7. SEM/SEI observations of AA2024-T3 sample surface after CP measurements; (a,b) BM and (c,d) fLSPed sample.

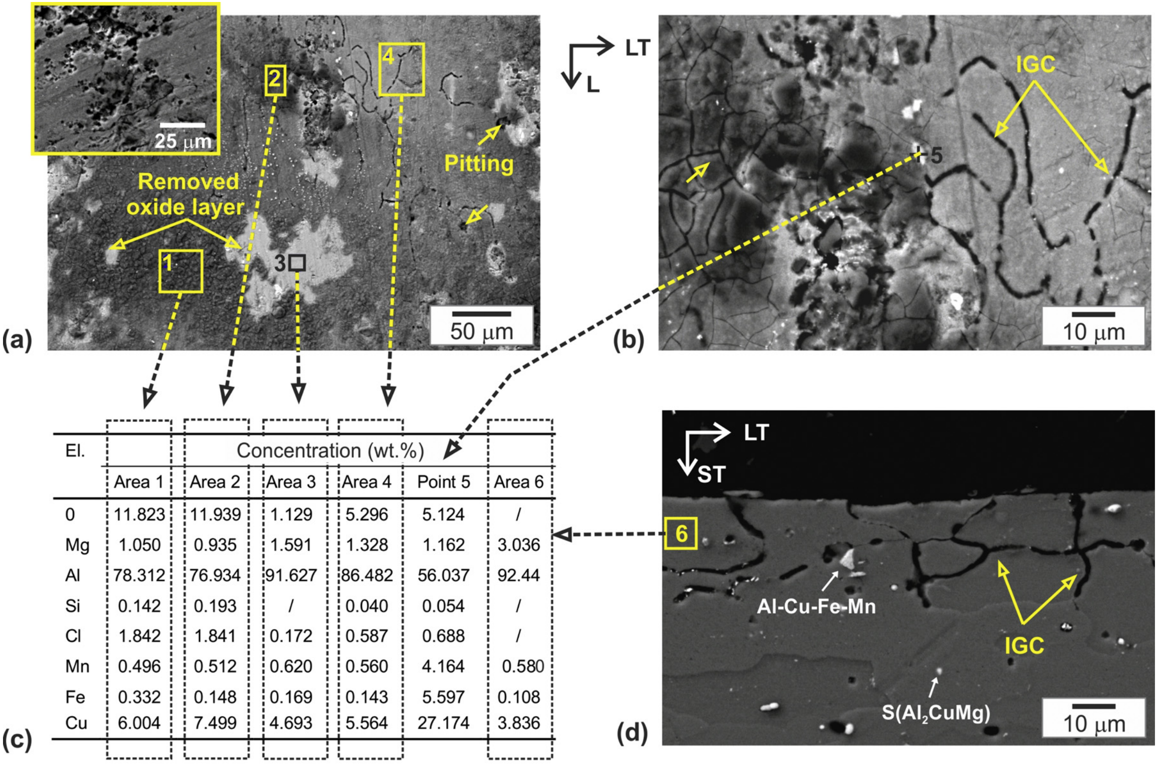

El.	Concentration (wt.%)					
	Area 1	Area 2	Area 3	Area 4	Point 5	Area 6
0	11.823	11.939	1.129	5.296	5.124	/
Mg	1.050	0.935	1.591	1.328	1.162	3.036
Al	78.312	76.934	91.627	86.482	56.037	92.44
Si	0.142	0.193	/	0.040	0.054	/
Cl	1.842	1.841	0.172	0.587	0.688	/
Mn	0.496	0.512	0.620	0.560	4.164	0.580
Fe	0.332	0.148	0.169	0.143	5.597	0.108
Cu	6.004	7.499	4.693	5.564	27.174	3.836

Fig. 8. (a,b) SEM/BEI observations of BM surface after the CP, (c) EDS results corresponding to the specific regions and (d) metallographic cross-section (LT–ST plane) showing intergranular attack.

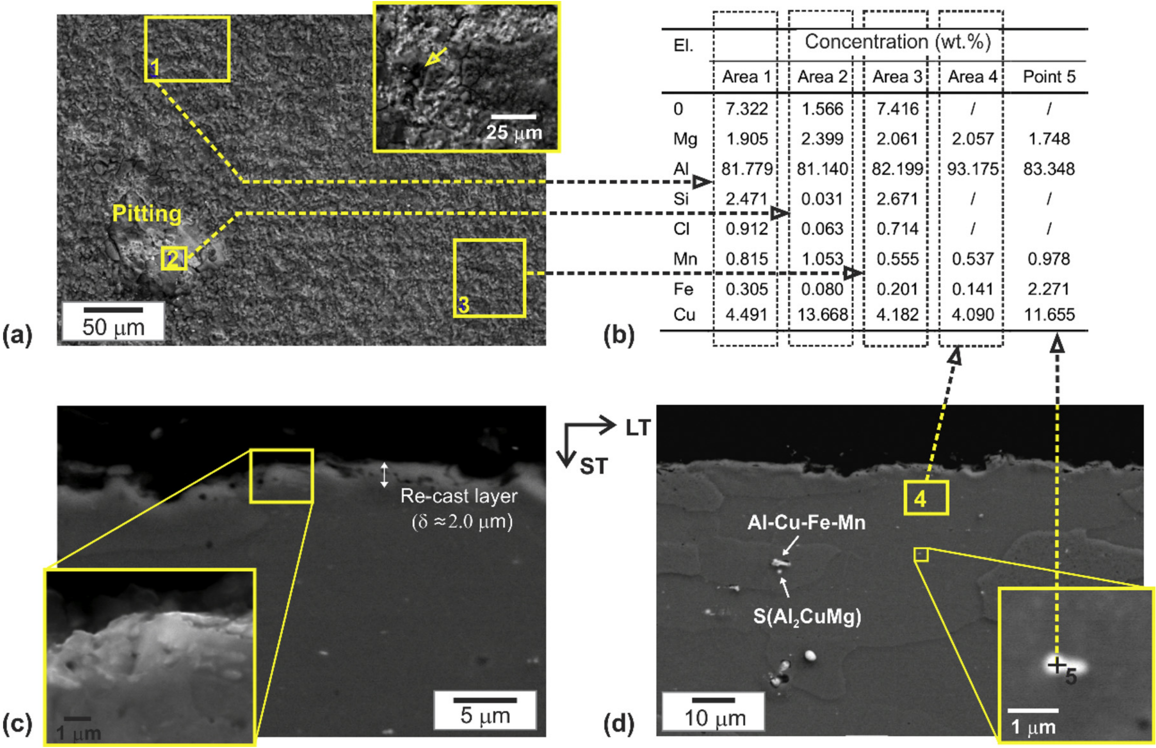

El.	Concentration (wt.%)				
	Area 1	Area 2	Area 3	Area 4	Point 5
0	7.322	1.566	7.416	/	/
Mg	1.905	2.399	2.061	2.057	1.748
Al	81.779	81.140	82.199	93.175	83.348
Si	2.471	0.031	2.671	/	/
Cl	0.912	0.063	0.714	/	/
Mn	0.815	1.053	0.555	0.537	0.978
Fe	0.305	0.080	0.201	0.141	2.271
Cu	4.491	13.668	4.182	4.090	11.655

Fig. 9. (a) SEM/BEI observation of fLSPed surface after the CP, (b) EDS results of the specific regions, (c,d) metallographic cross-section (LT–ST plane) showing the top recast surface layer.

evenly distributed constituent particles within the Al matrix at the surface. Moreover, it should be noted that with precipitation-hardenable alloys, such as the AA2024 alloy, the size and distribution of the intermetallic precipitates depends on the quenching and artificial ageing conditions. Thus, the continuous precipitation of intermetallics at grain boundaries can be reduced [34]. Hence, IGC can attack can be reduced or prevented in both peak-aged and over-aged AA2024 samples due to dislocation pile-ups, which prevent the diffusion of super-saturated solutes into the grain boundaries and continuous S-phase precipitation [9].

Although the fLSPed sample had the same nominal composition and microstructure, local chemical composition and grain boundaries at the top surface were altered by SPD, high density dislocations [24] and sequential melting/rapid cooling and deposition of the recast material during fLSP treatment, which can contribute to higher charge-transfer resistance R_{ct} with reduced fractional area of the liquid–solid interface and corrosion activity. In addition, as can be seen in Fig.9c, the recast layer was negligibly small (~2 μm), homogeneous and with no cracks. Recently, Brunner et al. [7] investigated the corrosion resistance of ultrafine-grained AA2024-T351 produced by severe deformation using multiple-pass equal-channel angular pressing (ECAP) in a 0.5 M NaCl solution. These same authors confirmed mixing and re-distribution of S-phase particles and solute-depleted zones along with significant breakup of second-phase particles after the ECAP process. In addition, results have confirmed that grain-refined and homogenised microstructure with newly formed grain boundaries is not susceptible to IGC attack.

Surface morphology of the BM sample (Fig. 8a) also indicate numerous regions with removed passive/oxide film, which presumably occurred during polarization. EDS analysis results inside this region (Fig. 8c – area 3) depicted the highest amount of Al, with ~91 wt.%, and lowest oxygen content (~1 wt.%). Although, the passive/oxide film on Al has very low solubility and electronic conductivity in neutral, noncomplex solutions [66], the oxide film is thinner on the areas with numerous intermetallic phases beneath it. Hence, oxygen reduction and solubility of the oxide film occur in such cathodic areas [67]. In contrast, the fLSPed sample did not reveal this, indicating a more corrosion-resistant oxide film and a less active surface due to local surface melting, ablation and consecutive shock waves.

3.2.4. Electrochemical impedance spectroscopy

The corrosion resistance and durability in aggressive chloride solution was also examined by EIS studies after 1 h and 24 h immersion (pre-corroded sample after CP tests and exposure to air under ambient conditions for six months) in a 0.6 M NaCl solution at OCP. The EIS spectra are presented in Fig. 10, as Nyquist (a, c) and Bode plots (b, d). The Nyquist plot after 1 h immersion in 0.6 M NaCl in Fig. 10a confirms the conclusion, drawn from the wettability data, LPR and CP tests about the significant influence of fLSP towards a more efficient, corrosion resistant surface. It can be clearly seen from the Bode plot in Fig.10b that much lower corrosion resistance is obtained with the untreated, BM AA2024-T3 sample, with a smaller diameter capacitance loop and lower, less stable and lower absolute impedance value $|Z|$ at low frequency range with smaller phase angle maxima across a wider frequency range compared to the fLSPed sample.

The EIS spectra after 24 h immersion (Fig.10c and d) which were performed on pre-corroded samples (after CP + 6 months exposure at ambient conditions) indicate an increased diameter of the capacitance loop with the BM sample, and a new relaxation process at high frequency, which is most probably explained by a porous corrosion product layer and its thickening [19]. In contrast, the fLSPed sample showed similar behaviour regardless of the immersion time in the test solution, with improved long-term stability even when corrosion had been initiated. Moreover, Bode plots in Fig. 10b and d show more stable, higher absolute impedance $|Z|$ values with higher, more stable phase angle maxima across a wider frequency range.

For a more detailed analysis and a deeper discussion of corrosion behaviour, the EIS results were fitted using ($R_s[Q_f(R_f(Q_{dl}R_{ct})])$ equivalent electrical circuit (EEC), which is presented as an inset in Fig. 10. Although the fitted line of EIS spectra in Fig. 10b show some deviations

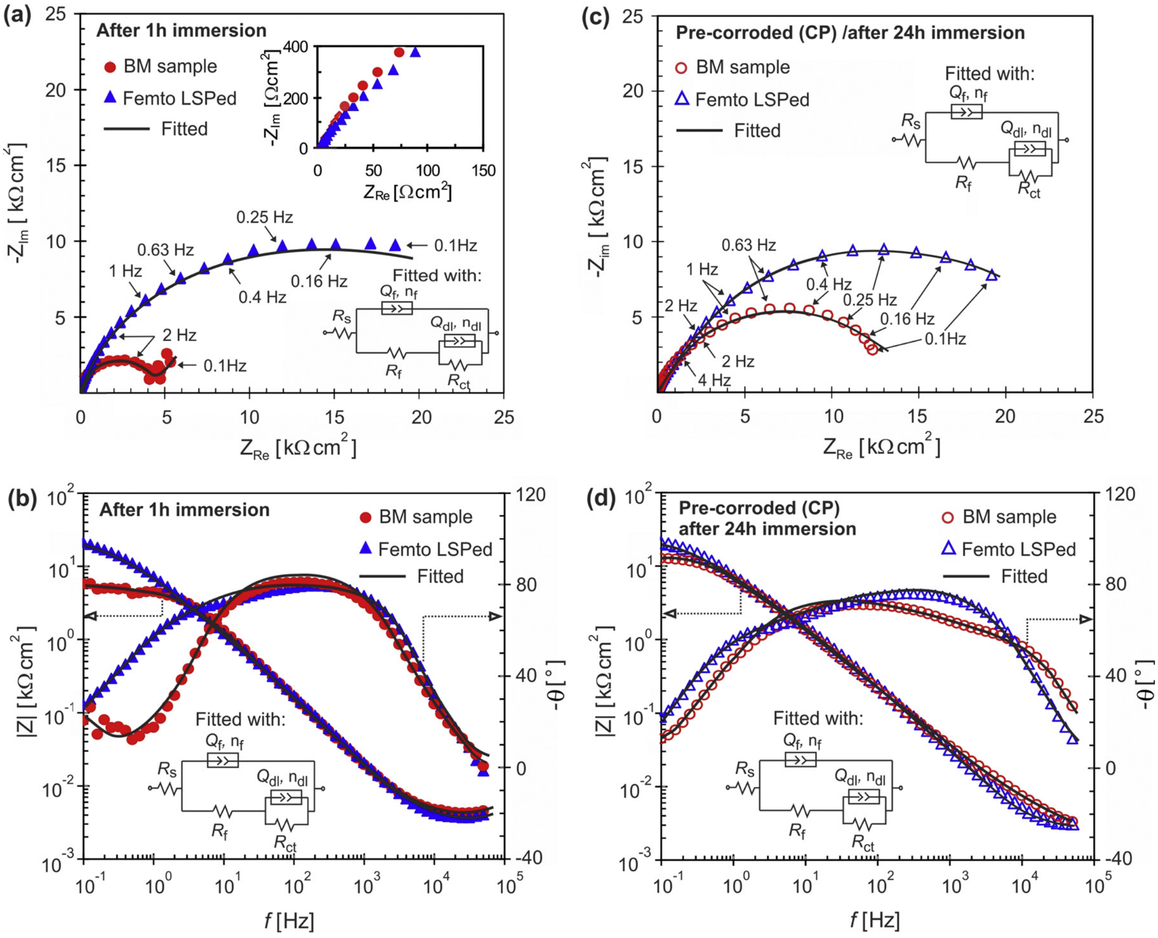

Fig. 10. EIS spectra presented as (a,c) Nyquist and (b,d) Bode plots after (a,b) 1 h and (c, d) 24 h immersion (pre-corroded samples after CP and exposure to ambient for six months).

Table 3

Circuit parameters for AA2024-T3 samples obtained from simulation of EIS measurements using EEC.

Parameter	Uncorroded samples after 1 h immersion in 0.6 M NaCl		Pre-corroded samples (after CP) after 24 h immersion in 0.6 M NaCl	
	BM	fLSPed	BM	fLSPed
R_s [Ωcm^2]	4.15	3.64	2.63	2.73
Q_f [Scm^{-2} s^n]	13.9×10^{-6}	7.39×10^{-6}	6.54×10^{-6}	13.2×10^{-6}
n-(Q_f) [/]	0.94	1	0.91	0.80
C_f [Fcm^{-2}]	11.8×10^{-6}	7.39×10^{-6}	2.67×10^{-6}	5.85×10^{-6}
R_f [Ωcm^2]	4.74×10^3	140	30.42	2.88×10^3
Q_{dl} [Scm^{-2} s^n]	68.9×10^{-5}	2.53×10^{-5}	1.99×10^{-5}	1.80×10^{-5}
n-(Q_{dl}) [/]	1	0.67	0.76	0.82
C_{dl} [Fcm^{-2}]	68.9×10^{-5}	2.20×10^{-5}	1.34×10^{-5}	1.49×10^{-5}
R_{ct} [Ωcm^2]	0.53×10^4	3.01×10^4	1.47×10^4	2.34×10^4
R_t [Ωcm^2]	1.01×10^4	3.02×10^4	1.47×10^4	2.63×10^4

compared to the experimental data in the low/low-to-mid frequency ranges, the obtained fitting results are in good accordance with other studies in the recent corrosion literature [21,68,69]. The chosen EEC, along with the constant phase elements (Q-CPE), was used due to the best fitting and smallest error ($\chi = 2.29 \times 10^{-4}$ to 2.65×10^{-3}). The oxide film (C_f) and double-layer (C_{dl}) capacitances were calculated from the CPE (Q/n) and resistance R (of the specific group) by $C = (QR)^{1/n}/R$ [34,69]; a detailed description and definition of the specific circuit element are given in full in our recent work [51]. Extracted EIS data from the equivalent circuit are shown in Table 3.

EIS results after 1 h immersion indicated the presence of barrier-type oxide film on both, i.e. BM and fLSPed samples, with similar impedance-associated capacitive response in the Bode spectra. However, the fLSPed sample confirmed a 1.6-times smaller barrier-type oxide film capacitance C_f compared to the untreated sample (7.39 μFcm^{-2} vs. 11.8 μFcm^{-2}). Moreover, the double-layer capacitance C_{dl} decreased more than 30-times (22 μFcm^{-2} vs. 689 μFcm^{-2}), and charge-transfer resistance R_{ct} increased more than 5-times (30.1 $k\Omega cm^2$ vs. 5.33 $k\Omega cm^2$) after fLSP treatment. These results suggest that the fLSP treatment in the presence of chlorides contributes to a partial blockage of the active areas, which offers a more corrosion-resistant surface.

EIS spectra obtained after 24 h immersion on pre-corroded samples also showed similar capacitive slopes for both samples. However, due to the presence of an additional element (porous corrosion product film) in the case of the BM sample C_f decreased 4-times, which is in accordance with results from Fig. 8 (EDS results of region 1 & 2). This is also confirmed by the film resistance R_f, which decreased for the BM sample from 4.74 $k\Omega cm^2$ to only 30.42 Ωcm^2. In contrast, the R_f of the fLSPed sample increased sharply from 140 Ωcm^2 to 2.88 $k\Omega cm^2$, which indicates a more resistant oxide film compared to the BM sample.

Furthermore, by comparing the changes of the total resistance R_t ($R_t = R_f + R_{ct}$) and double-layer capacitance C_{dl} of BM and fLSPed samples after different immersion times, it can clearly be seen that with fLSP treatment the changes were much smaller than for the BM sample, indicating a durable, corrosion-resistant surface with reduced corrosion kinetics. Although the total resistance R_t of the BM sample increased with pre-corroded sample after longer immersion in the solution, R_t was still 1.8-times lower than for the fLSPed sample (14.7 $k\Omega cm^2$ vs. 26.3

kΩ m^2); hence, the fLSPed surface can also inhibit the corrosion process on pre-corroded samples with longer immersion in chloride solution.

4. Conclusions

Femto second laser shock peening (fLSP) without a sacrificial overlay under atmospheric conditions with no confining medium was confirmed as an effective method to induce high compressive residual stress and increased hardness in the treated, top-surface layer. Moreover, a hierarchical superhydrophobic surface ($SCA = 160 \pm 4°$) with almost negligible roughness increased and improved corrosion behaviour in a 0.6 M NaCl test solution.

OCP results during 1 h immersion confirmed potential ennoblement of the fLSPed sample, whereas during longer 24 h immersion time on pre-corroded samples after CP, reduced corrosion activity was also confirmed, with improved long-term stability of fLSPed surface, due to more resistant oxide film. LPR and CP results confirmed 18-times higher polarization resistance R_p (34.83 kΩcm^2 vs. 1.92 kΩcm^2) and 4-times lower corrosion current density i_{corr} (1.95 μAcm–^{2} vs. 0.49 μAcm–^{2}) for the fLSPed sample. Moreover, a lower degree of anodic dissolution, improved and faster repassivation, with more than 150% higher $\Delta E/\Delta i$ gradient was confirmed for the fLSPed sample, indicating much lower anodic dissolution in aggressive Cl$^-$ solution.

SEM/EDS analyses of the BM sample revealed extensive, widespread localised pitting and IGC attack. In contrast, for the fLSPed sample the pitting attack was confined to a few isolated regions, whereas the initiation of IGC was completely eradicated due to reduced fractional area of liquid–solid interface and a more homogeneous, refined microstructure with evenly distributed constituent particles, which prevented the 'chain-link' IGC effect. In addition, EIS results demonstrated good corrosion inhibitive properties of the fLSPed sample, similar to the LPR and CP results, with higher total resistance. Moreover, EIS results have shown similar behaviour of 'fresh' and pre-corroded fLSPed samples, with smaller variations of circuit parameters than the BM sample, indicating a durable surface with improved long-term stability against corrosion in a chloride environment.

Data availability

The raw/processed data required to reproduce these findings cannot be shared at this time as the data also forms part of an ongoing study.

Acknowledgements

The authors acknowledge the financial support from the state budget by the Slovenian Research Agency Programme No. P2-0270. This work was supported in part by JSPS KAKENHI Grant Numbers JP16H04247 and JP16K14417, by Amada Foundation Grant Numbers AF-2016217 and by the ImPACT Program of Council for Science, Technology and Innovation (Cabinet Office, Government of Japan). The authors would like to thank Dr. P. Gregorčič for providing surface wettability, i.e. contact angle measurements. The authors would also like to thank Prof. Akio Hirose and Mr. Takafumi Eimura for valuable comments, discussion and support for femtosecond laser peening experiments and surface characteristics, respectively.

References

[1] V. Guillaumin, G. Mankowski, Localized corrosion of 2024 T351 aluminium alloy in chloride media, Corros. Sci. 41 (1999) 421–438.
[2] S. Borojević, D. Lukić, M. Milošević, J. Vukman, D. Kramar, Adv. Prod. Eng. Manag. 13 (2) (2018) 125–135.
[3] J.R. Davis, Corrosion of Aluminum and Aluminum Alloys, 1st ed., ASM International, Metals Park, OH, 1999.
[4] N.L. Sukiman, X. Zhou, N. Birbilis, A.E. Hughes, J.M.C. Mol, S.J. Garcia, X. Zhou, G.E. Thompson, Durability and corrosion of aluminium and its alloys: overview, property space, techniques and developments, in: Z. Ahmad (Ed.), Aluminium Alloys—New Trends in Fabrication and Applications, IntechPublications, Rijeka, 2012, pp. 47–97.
[5] N. Birbilisa, Y.M. Zhu, S.K. Kairy, M.A. Glenn, J.-F. Nie, A.J. Morton, Y. Gonzalez-Garcia, H. Terryn, J.M.C. Mol, A.E. Hughes, A closer look at constituent induced localised corrosion in Al-Cu-Mgalloys, Corros. Sci. 113 (2016) 160–171.
[6] G.O. Ilevbare, O. Schneider, R.G. Kelly, J.R. Scully, In situ confocal laser scanning microscopy of AA2024-T3 corrosion metrology I. Localized corrosion of particles, J. Electrochem. Soc. 151 (2004) 453–464.
[7] J.G. Brunner, N. Birbilis, K.D. Ralston, S. Virtanen, Impact of ultrafine–grained microstructure on the corrosion of aluminium alloy AA2024, Corros. Sci. 57 (2012) 209–214.
[8] M.-L. de Bonfils-Lahovary, L. Laffont, C. Blanc, Characterization of intergranular corrosion defects in a 2024 T351aluminium alloy, Corros. Sci. 119 (2017) 60–67.
[9] Z. Wang, P. Chen, H. Li, B. Fang, R. Song, Z. Zheng, The intergranular corrosion susceptibility of 2024 Al alloy during re–ageing after solution treating and cold–rolling, Corros. Sci. 114 (2017) 156–168.
[10] R.G. Buchheit, A compilation of corrosion potentials reported for intermetallic phases in aluminum alloys, J. Electrochem. Soc. 142 (11) (1995) 3994–3996.
[11] X.Zhang T. Hashimoto, J. Lindsay, X. Zhou, Investigation of the de-alloying behaviour of θ-phase (Al_2Cu) in AA2024-T351 aluminium alloy, Corros. Sci. 108 (2016) 85–93.
[12] R.G. Buchheit, R.P. Grant, P.F. Hiava, B. Mckenzie, G.L. Zender, Local Dissolution Phenomena Associated with S Phase (Al_2CuMg) Particles in Aluminum Alloy 2024-T3, J. Electrochem. Soc. 144 (8) (1997) 2621–2628.
[13] R.G. Buchheit, N. Birbilis, Electrochemical microscopy: an approach for understanding localized corrosion in microstructurally complex metallic alloys, Electrochim. Acta 55 (27) (2010) 7853–7859.
[14] J. Li, N. Birbilis, R.G. Buchheit, Electrochemical assessment of interfacial characteristics of intermetallic phases present in aluminium alloy 2024-T3, Corros. Sci. 101 (2015) 155–164.
[15] J.M.C. Mol, A.E. Hughes, B.R.W. Hinton, S. van der Zwaag, A morphological study of filiform corrosive attack on chromated and alkaline-cleaned AA2024-T351 aluminium alloy, Corros. Sci. 46 (2004) 1201–1224.
[16] A.K. Chattopadhyay, M.K.R. Zentner, Aerospace and aircraft coatings, Fed. Soc. For. Coat. Technol. (1990).
[17] A.E. Hughes, J.M.C. Mol, B.R.W. Hinton, S. van der Zwaag, A morphological study of filiform corrosive attack on cerated AA2024-T351 aluminium alloy, Corros. Sci. 47 (2005) 107–124.
[18] T.H. Muster, H. Sullivan, D. Lau, D.L.J. Alexander, N. Sherma, S.J. Garcia, T.G. Harvey, T.A. Markley, A.E. Hughes, P.A. Corrigan, A.M. Glenn, P.A. White, S.G. Hardin, J. Mardel, J.M.C. Mol, A combinatorial matrix of rare earth chloride mixtures as corrosion inhibitors of AA2024-T3: Optimisation using potentiodynamic polarisation and EIS, Electrochim. Acta 67 (2012) 95–103.
[19] H. Shi, E.-H. Han, F. Liu, Corrosion protection of aluminium alloy 2024-T3 in 0.05 M NaCl by cerium cinnamate, Corros. Sci. 53 (2011) 2374–2384.
[20] T.H. Muster, D. Lau, H. Wrubel, N. Sherman, A.E. Hughes, T. Harvey, T. Markley, D.L.J. Alexander, P. Corrigan, P.A. White, S.G. Hardin, M.A. Glenn, J. Mardel, S.J. Garcia, J.M.C. Mol, An investigation of rare earth chloride mixtures: combinatorial optimisation for AA2024-T3 corrosion inhibition, Surf. Interface Anal. 42 (2010) 170.
[21] O. Jilani, N. Njah, P. Ponthiaux, Transition from intergranular to pitting corrosion in fine grained aluminum processed by equal channel angular pressing, Corros. Sci. 87 (2014) 259–264.
[22] A.H. Clauer, J.H. Holbrook, B.P. Fairand, Shock Waves and High-Strain-Rate Phenomena in Metals, Plenum Publishing Corporation, New York, 1981, pp. 675–703.
[23] R. Fabbro, P. Peyre, L. Berthe, X. Scherpereel, Physics and applications of laser shock processing, Med. Laser Appl. 10 (1998) 265–279.
[24] T. Sano, T. Eimura, R. Kashiwabara, T. Matsuda, Y. Isshiki, A. Hirose, Femtosecond laser peening of 2024 aluminum alloy without a sacrificial overlay under atmospheric conditions, J. Laser Appl. 29 (2017) 012005, , https://doi.org/10.2351/1.4967013.
[25] C. Correa, D. Peral, J.A. Porro, M. Díaz, L. Ruiz de Lara, A. García-Beltrán, et al., Random-type scanning patterns in laser shock peening without absorbing coating in 2024-T351 Al alloy: a solution to reduce residual stress anisotropy, Opt. Laser Technol. 73 (2015) 179–187.
[26] U. Trdan, J.A. Porro, J.L. Ocaña, J. Grum, Laser shock peening without absorbent coating (LSPwC) effect on 3D surface topography and mechanical properties of 6082-T651 Al alloy, Surf. Coat. Technol. 208 (2012) 109–116.
[27] D. Kumar, S.N. Akhtar, A.K. Patel, J. Ramkumar, K. Balani, Tribological performance of laser peened Ti–6Al–4V, Wear 322–323 (2015) 203–217.
[28] I. Yakimets, C. Richard, G. Béranger, P. Peyre, Laser peening processing effect on mechanical and tribological properties of rolling steel 100Cr6, Wear 256 (2004) 311–320.
[29] P. Peyre, R. Fabbro, P. Merrien, H.P. Lieurade, Laser shock processing of aluminium alloys. Application to high cycle fatigue behaviour, Mater. Sci. Eng. A 210 (1996) 102–113.
[30] Y. Sano, K. Masaki, T. Gushi, T. Sano, Improvement in fatigue performance of friction stir welded A6061-T6 aluminum alloy by laser peening without coating, Mater. Des. 36 (2012) 809–814.
[31] N. Kashaev, V. Ventzke, M. Horstmann, S. Chupakhin, S. Riekehr, R. Falck, E. Maawad, P. Staron, N. Schell, N. Huber, Effects of laser shock peening on the microstructure and fatigue crack propagation behaviour of thin AA2024 specimens, Int. J. Fatigue 98 (2017) 223–233.
[32] E. Maawad, Y. Sano, L. Wagner, H.-G. Brokmeier, Ch. Genzel, Investigation of laser shock peening effects on residual stress state and fatigue performance of titanium alloys, Mater. Sci. Eng. A 536 (2012) 82–91.

[33] A. Telang, A.S. Gill, S. Teysseyre, S.R. Mannava, D. Qian, V.K. Vasudevan, Effects of laser shock peening on SCC behavior of Alloy 600 in tetrathionate solution, Corros. Sci. 90 (2015) 434–444.

[34] U. Trdan, J. Grum, SEM/EDS characterization of laser shock peening effect on localized corrosion of Al alloy in a near natural chloride environment, Corros. Sci. 82 (2014) 328–338.

[35] D. Karthik, S. Swaroop, Laser shock peening enhanced corrosion properties in a nickel based Inconel 600 superalloy, J. Alloys 694 (2016) 1309–1319.

[36] U. Trdan, J. Grum, Evaluation of corrosion resistance of AA6082-T651 aluminium alloy after laser shock peening by means of cyclic polarisation and ElS methods, Corros. Sci. 59 (2012) 324–333.

[37] J.Z. Lu, H. Qi, K.Y. Luo, M. Luo, X.N. Cheng, Corrosion behaviour of AISI 304 stainless steel subjected to massive laser shock peening impacts with different pulse energies, Corros. Sci. 80 (2014) 53–59.

[38] D. Karthik, S. Arul Xavier Stango, U. Vijayalakshmi, S. Swaroop, Electrochemical behavior of laser shock peened Inconel 625 superalloy, Surf. Coat. Technol. 311 (2017) 46–54.

[39] U. Trdan, M. Skarba, J. Grum, Laser shock peening effect on the dislocation transitions and grain refinement of Al–Mg–Si alloy, Mater. Charact. 97 (2014) 57–68.

[40] H. Krawiec, V. Vignal, H. Amar, P. Peyre, Local electrochemical impedance spectroscopy study of the influence of ageing in air and laser shock processing on the micro-electrochemical behaviour of AA2050-T8 aluminium alloy, Electrochim. Acta 56 (2011) 9581–9587.

[41] D. Karthik, S. Swaroop, Effect of laser peening on electrochemical properties of titanium stabilized 321 steel, Mater. Chem. Phys. 193 (2017) 147–155.

[42] R. Evans, A.D. Badger, F. Fallie`s, M. Mahdieh, T.A. Hall, P. Audebert, J.-P. Geindre, J.-C. Gauthier, A. Mysyrowicz, G. Grillon, A. Antonetti, Time- and space-resolved optical probing of femtosecondlaser-driven shock waves in aluminum, Phys. Rev. Lett. 77 (1996) 3359–3362.

[43] M. Tsujino, T. Sano, O. Sakata, N. Ozaki, S. Kimura, S. Takeda, M. Okoshi, N. Inoue, R. Kodama, K.F. Kobayashi, A. Hirose, Synthesis of submicron metastable phase of silicon using femtosecond laser-driven shock wave, J. Appl. Phys. 110 (2011) 126103.

[44] T. Sano, H. Mori, E. Ohmura, I. Miyamoto, Femtosecond laser quenching of the ε phase of iron, J. Appl. Phys. Lett. 83 (2003) 349.

[45] T. Matsuda, T. Sano, K. Arakawa, A. Hirose, Dislocation structure produced by an ultrashort shock pulse, J. Appl. Phys. 116 (2014) 183506.

[46] T. Matsuda, T. Sano, K. Arakawa, A. Hirose, Multiple-shocks induced nanocrystallization in iron, Appl. Phys. Lett. 105 (2014) 021902.

[47] A.M. Kietzig, S.G. Hatzikiriakos, P. Englezos, Patterned superhydrophobic metallic surfaces, Langmuir 25 (2009) 4821–4827.

[48] A.Y. Vorobyev, C. Guo, Multifunctional surfaces produced by femtosecond laser pulses, J. Appl. Phys. 117 (2015) 033103.

[49] P. Gregorčič, B. Šetina-Batič, M. Hočevar, Controlling the surface wettability by nanosecond direct laser texturing at high fluences, Appl. Phys. A (2017) 123–766.

[50] U. Trdan, M. Hočevar, P. Gregorčič, Transition from superhydrophilic to superhydrophobic state of laser textured stainless steel surface and its effect on corrosion resistance, Corros. Sci. 123 (2017) 21–26.

[51] D. Ravnikar, R. Shanker Rajamure, U. Trdan, N.B. Dahotre, J. Grum, Electrochemical and DFT studies of laser-alloyed TiB2/TiC/Al coatings on aluminium alloy, Corros. Sci. 136 (2018) 18–27.

[52] D. Wallinder, J. Pan, C. Leygraf, A. Delblanc-Bauer, EIS and XPS study of surface modication of 316L stainless steel after passivation, Corros. Sci. 41 (1999) 275–289.

[53] U. Trdan, M. Skarba, J.A. Porro, J.L. Ocaña, J. Grum, Application of massive laser shock processing for improvement of mechanical and tribological properties, Surf. Coat. Technol. 342 (2018) 1–11.

[54] M.A. Abdulstaar, K.J. Al-Fadhalah, L. Wagner, Microstructural variation through weld thickness and mechanical properties of peened friction stir welded 6061 aluminum alloy joints, Mater. Charact. 126 (2017) 64–73.

[55] R.S. Rajamure, H.D. Vora, S.G. Srinivasan, N.B. Dahotre, Laser alloyed Al-W coatings on aluminum for enhanced corrosion resistance, Appl. Surf. Sci. 328 (2015) 205–214.

[56] A.B.D. Cassie, S. Baxter, Wettability of porous surfaces, Trans. Faraday Soc. 40 (1944) 0546–0550.

[57] L. Ruiz de Lara, R. Jagdheesh, J.L. Ocaña, Corrosion resistance of laser patterned ultrahydrophobic aluminium surface, Mater. Lett. 184 (2016) 100–103.

[58] G. McHale, N.J. Shirtcliffe, M.I. Newton, Super-hydrophobic and super-wetting surfaces: analytical potential, Analyst 129 (2004) 284–287.

[59] R.N. Wenzel, Resistance of solid surfaces to wetting by water, Ind. Eng. Chem. 28 (1936) 988–994.

[60] L.B. Boinovich, A.M. Emelyanenko, K.A. Emelyanenko, A.G. Domantovsky, A.A. Shiryaev, Comment on "Nanosecond laser textured superhydrophobic metallic surfaces and their chemical sensing applications" by Duong V. Ta, Andrew Dunn, Thomas J. Wasley, Robert W. Kay, Jonathan Stringer, Patrick J. Smith, Colm Connaughton, Jonathan D. Shephard (Appl. Surf. Sci. 357 (2015) 248-254), Appl. Surf. Sci. 379 (2016) 111–113.

[61] L.B. Boinovich, A.M. Emelyanenko, A.D. Modestov, A.G. Domantovsky, A.A. Shiryaev, K.A. Emelyanenko, O.V. Dvoretskaya, A.A. Ganne, Corrosion behavior of superhydrophobic aluminum alloy in concentrated potassium halide solutions: When the specific anion effect is manifested, Corros. Sci. 112 (2016) 517–527.

[62] A.Y. Vorobyev, C. Guo, Nanochemical effects in femtosecond laser ablation of metals, Appl. Phys. Lett. 102 (2013) 074107.

[63] W.H. Ailor (Ed.), Handbook on Corrosion Testing and Evaluation, John Wiley and Sons, Inc., New York, 1971, p. 174.

[64] ASTM Standard G59-97, Standard Test Method for Conducting Potentiodynamic Polarization Resistance Measurements, ASTM International, West Conshohocken, PA, 2009, https://doi.org/10.1520/G0059-97R09 http://www.astm.org.

[65] Z. Bergant, U. Trdan, J. Grum, Effect of high-temperature furnace treatment on the microstructure and corrosion behavior of NiCrBSi flame-sprayed coatings, Corros. Sci. 88 (2014) 372–386.

[66] Z. Szklarska-Smialowska, Pitting corrosion of aluminum, Corros. Sci. 41 (1999) 1742–1767.

[67] C. Vargel, Corrosion of Aluminium, Elsevier Science, USA, 2004.

[68] P. Visser, H. Terryn, J.M.C. Mol, On the importance of irreversibility of corrosion inhibitors for active coating protection of AA2024-T3, Corros. Sci. 140 (2018) 272–285.

[69] Z. Davoodi, M. Esfahani Sarvghad, Microstructure and corrosion characterization of the interfacial regionin dissimilar friction stir welded AA5083 to AA7023, Corros. Sci. 107 (2016) 133–144.